

# New Measurements of the Motion of the Zodiacal Dust

R. J. Reynolds and G. J. Madsen

*Department of Astronomy, 475 N. Charter Street, University of Wisconsin–Madison,  
Madison, WI 53706*

`reynolds@astro.wisc.edu; madsen@astro.wisc.edu`

and

S. H. Moseley

*Code 685, Infrared Astrophysics Branch, Goddard Space Flight Center, Greenbelt, MD  
20771*

`moseley@stars.gsfc.nasa.gov`

## ABSTRACT

Using the Wisconsin H-Alpha Mapper (WHAM), we have measured at high spectral resolution and high signal-to-noise the profile of the scattered solar Mg I  $\lambda 5184$  absorption line in the zodiacal light. The observations were carried out toward 49 directions that sampled the ecliptic equator from solar elongations of  $48^\circ$  (evening sky) to  $334^\circ$  (morning sky) plus observations near  $+47^\circ$  and  $+90^\circ$  ecliptic latitude. The spectra show a clear prograde kinematic signature that is inconsistent with dust confined to the ecliptic plane and in circular orbits influenced only by the sun's gravity. In particular, the broadened widths of the profiles, together with large amplitude variations in the centroid velocity with elongation angle, indicate that a significant population of dust is on eccentric orbits. In addition, the wide, flat-bottomed line profile toward the ecliptic pole indicates a broad distribution of orbital inclinations extending up to about  $30^\circ$ – $40^\circ$  with respect to the ecliptic plane. The absence of pronounced asymmetries in the shape of the profiles limits the retrograde population to less than 10% of the prograde population and also places constraints on the scattering phase function of the particles. These results do not show the radial outflow or evening–morning velocity amplitude asymmetry reported in some earlier investigations. The reduction of the spectra included the discovery and removal of extremely faint, unidentified terrestrial emission lines that contaminate and distort the underlying Mg I profile. This atmospheric emission is too weak to have been seen in earlier, lower signal-to-noise observations, but it probably affected the line centroid measurements of previous investigations.

*Subject headings:* interplanetary medium—line: profiles—scattering—solar system: general

## 1. INTRODUCTION

The motion of the interplanetary dust particles orbiting the sun contains clues about their origin and the nongravitational forces affecting their lifetimes in the solar system, with potential relevance to dust disks surrounding other stars (e.g., Mann, Grün, & Wilck 1996; Dermott et al. 1994). A more accurate understanding of this “zodiacal cloud” can also impact studies of faint Galactic and extragalactic backgrounds (e.g., Haffner et al. 2003; Bernstein, Freedman, & Madore 2002; Kelsall et al. 1998). In theory, Doppler shifts of scattered solar Fraunhofer lines in the zodiacal light provide an opportunity to explore and monitor the large-scale kinematics of interplanetary dust in the inner solar system through ground-based spectroscopic techniques (e.g., Ingham 1963; James 1969, 1996; Hirchi & Beard 1987; Clarke et al. 1996), which would be an important complement to studies of the zodiacal brightness distribution and the *in situ* detection of interplanetary particles by spacecraft (Mann 1998; Grün et al. 1997). In practice, the faint, spatially extended nature of the zodiacal light, combined with the requirements of both high signal-to-noise and high spectral resolution to measure the predicted subtle changes in the position and shape of the line, have made these observations difficult to carry out.

Early attempts that targeted the H $\beta$   $\lambda$ 4861 line (e.g., Clarke et al. 1967; Daehler et al. 1968; Reay & Ring 1969) encountered the additional problem that the absorption line was severely contaminated by emission originating from atomic hydrogen in the earth’s atmosphere and the Galaxy’s interstellar medium (Reynolds, Roesler, & Scherb 1973). This led investigators to concentrate their observations on other lines (James & Smeethe 1970; Hicks, May, & Reay 1974; Fried 1978; East & Reay 1984), especially the Mg I line at 5183.62 Å, which has a large equivalent width and seemed to have no contaminating atmospheric emission. However, except for the conclusion that the motion was primarily prograde, the resulting information about the orbital properties of the dust was uncertain and contradictory (see a summary of the situation by Clarke et al. 1996).

One of the principal difficulties with these earlier observations was the insufficient throughput of the spectrometers. This resulted in low signal-to-noise data and thus prevented precise measurements of line centroids and shapes, particularly at large solar elongations and at high ecliptic latitudes, where the zodiacal emission is faintest, but where observations are crucial for comparisons with predictions of kinematic models. Below, we present new, high signal-to-noise observations of the Mg I  $\lambda$ 5184 line in the zodiacal light using the Wisconsin

H $\alpha$  Mapper (WHAM) Fabry-Perot facility at the National Optical Astronomy Observatory on Kitt Peak in Arizona. WHAM’s unprecedented combination of high throughput and high spectral resolution reveal clearly resolved Mg I line profiles that are shifted and broadened by the motion of the zodiacal dust.

## 2. THE WISCONSIN H $\alpha$ MAPPER (WHAM) OBSERVATIONS

WHAM consists of a 15 cm aperture, dual-etalon Fabry-Perot spectrometer coupled to a high efficiency CCD camera and fed by a dedicated 0.6 m telescope. The dual-etalon design, when compared to traditional single etalon Fabry-Perot systems, provides superior ghost and order rejection, extends the free spectral range, and suppresses the Lorentzian-like wings of the spectral response function. The CCD is used as a multichannel detector to record a 12 km s $^{-1}$  (0.2 Å at 5184 Å) resolution spectrum over a 200 km s $^{-1}$  (3.5 Å) spectral window that can be centered on any wavelength between 4800 Å and 7300 Å. The 15 cm diameter etalons provide maximum throughput, which when combined with the 0.6-m aperture telescope, results in a 1°.0 diameter beam on the sky.

Although built and operated primarily for studies of faint diffuse emission lines, particularly H $\alpha$  from the Galaxy’s interstellar medium, WHAM is ideally suited for high spectral resolution observations of any faint spatially extended source in the night sky, including comets (Morgenthaler et al. 2001), the earth’s atmosphere (Nossal et al. 2001), and the zodiacal light. The facility is completely remotely operated, and all the observations presented here were obtained with WHAM controlled from Madison, Wisconsin. Additional information about WHAM can be found in Haffner et al. (2003) and Tufte (1997).

Spectra centered on Mg I  $\lambda$ 5184 were obtained on the two moonless nights of 2002 November 4 and 2002 November 5. The spectra sample 49 directions near the ecliptic equator between elongations  $\epsilon = 47^\circ.5$  (evening sky) and  $\epsilon = 333^\circ.9$  ( $26^\circ.1$  west of the sun in the morning sky). Two directions at high ecliptic latitude were also observed,  $\epsilon \approx 272^\circ$ ,  $\beta \approx +47^\circ$  and the north ecliptic pole (NEP). In addition, observations of the relatively bright twilight sky were obtained to provide a calibration spectrum close to representing the unperturbed solar line profile. The directions of the zodiacal observations and the integration time for each spectrum are listed in the first three columns of Table 1. A  $30^\circ$  gap in the data near elongation  $225^\circ$  is due to interference by stars near the plane of the Milky Way, which produced anomalies in the spectra. The Galactic plane intersected the ecliptic plane at  $\epsilon = 50^\circ$  and  $\epsilon = 230^\circ$  at Galactic longitudes  $6^\circ$  and  $186^\circ$ , respectively.

A twilight spectrum is shown in Figure 1. The absorption feature is dominated by the

Mg I line at 5183.62 Å, with weak contributions from Fe I at 5184.27 Å and Cr I at 5184.59 Å, respectively. A potential problem in using twilight spectra to represent the unperturbed source spectrum is the contamination of the daylight and twilight Fraunhofer lines by a pseudo-continuum emission from inelastic scattering (i.e., rotational Raman scattering) of sunlight by atmospheric nitrogen and oxygen molecules. Both observations and theory suggest that this so-called “Ring effect” tends to fill in the Fraunhofer lines at about the 10% level with minimal change to the width of the line (e.g., Grainger & Ring 1962; Pallamraju, Baumgardner, & Chakrabarti 2000; Sioris & Evans 1999). To investigate this we compare our twilight spectrum in Figure 1 with a high resolution unscattered solar spectrum convolved with WHAM’s 12 km s<sup>-1</sup> wide spectral response profile. After scaling to match the “continua” and the profile minima within the observed spectral interval, we found the profiles to be nearly coincident (see Fig. 1). Thus both the twilight profile and the convolved direct solar profile appear to be good representations of the unperturbed solar spectrum and useful for comparison with the Doppler perturbed zodiacal profiles. The Ring effect, a phenomenon affecting the spectrum of sunlight that has been scattered by atmospheric molecules, is not relevant to the zodiacal light, which is scattered by interplanetary dust particles. Zero on the abscissa in Figure 1 and in all following spectra is defined by the centroid of the core of the Mg I component in the twilight spectra, with a small ( $\sim 0.2$  km s<sup>-1</sup>) correction for the observed Doppler shifts associated with the earth’s rotation. The uncertainty in this calibration is less than  $\pm 0.02$  Å ( $\pm 1$  km s<sup>-1</sup>).

### 3. THE ZODIACAL SPECTRA

#### 3.1. Contamination by Weak Atmospheric Emission Lines

The average spectrum east of the sun near  $\epsilon \approx 100^\circ$  and the average spectrum at the corresponding elongation west of the sun near  $\epsilon \approx 260^\circ$  are shown superposed in Figure 2a. The prograde kinematic signature of the zodiacal dust is clearly seen, with the profile in the evening spectrum (filled triangles) red shifted and the profile in the morning spectrum (filled circles) blue shifted with respect to the centroid of the unperturbed solar Mg I line. However, in addition to being shifted (and broadened), these spectra exhibit a number of extremely weak, relatively narrow emission lines. The fact that these emission features are present at the same wavelengths in both of the spectra in Figure 2a implies that they are not associated with the Doppler shifted light from the zodiacal dust and instead originate from the earth’s atmosphere. Previous studies of interstellar emission with WHAM have shown that such

weak (intensities  $\lesssim 0.1 R^1$ ), unidentified atmospheric emission lines are present throughout the visible spectrum (e.g., Hausen et al. 2002; Madsen et al. 2004, in prep). They distort the shapes of observed zodiacal and interstellar line profiles, modify their measured intensities and equivalent widths, and in observations with insufficient spectral resolution produce a pseudo-continuum of order  $10^{-8}$  erg cm $^{-2}$  s $^{-1}$  sr $^{-1}$  Å $^{-1}$ . Therefore, before proceeding with the analysis of the zodiacal line profiles, it was necessary to remove this contaminating terrestrial emission from each spectrum.

To characterize more accurately the spectrum of this foreground emission, all spectra in directions with the faintest zodiacal emission (i.e.,  $88^\circ < \epsilon < 272^\circ$ ) were averaged together, producing the very high signal-to-noise composite spectrum in Figure 2b, where all the zodiacal absorption features, including the Fe and Cr lines, are highly Doppler broadened into a single, smooth profile. From this spectrum it was possible to identify the narrow terrestrial emission features against the underlying, Doppler smeared zodiacal spectrum by fitting a smooth, single-gaussian profile to the spectrum in Figure 2b in such a way that the residuals were near zero or positive at all velocities. The residuals, indicated by the solid line in Figure 2c, then represent the spectrum of the foreground terrestrial emission. The sharpness of the features in Figure 2c provides additional confirmation that they are not associated with the highly broadened zodiacal profile. Also plotted in Figure 2c are the maximum and minimum allowed terrestrial emission spectra that are consistent with the spectrum in Figure 2b.

Although too weak to have been identified in earlier, lower signal-to-noise observations, this terrestrial emission, if not removed, would clearly distort the apparent centroid and shape of the underlying zodiacal absorption feature (see Fig. 4a below). Therefore, to obtain uncontaminated zodiacal profiles, we subtracted the best fitted terrestrial emission spectrum (solid line in Fig. 2c) from each of the spectra listed in Table 1. This process treated each spectrum the same and did not take into account possible temporal variations in the intensity of this emission or variations in the relative strengths of the individual emission components. However, because the emission is extremely weak, there was no way to identify and remove it from each spectrum independently. When the observations were separated by halves of the night, by day, and by high and low ecliptic latitude, the “best fit” spectrum in Figure 2c provided good removal of the emission features within the uncertainties, suggesting that this spectrum fairly approximates the terrestrial contamination in each individual spectrum.

---

<sup>1</sup>1 R =  $10^6/4\pi$  photons s $^{-1}$  cm $^{-2}$  sr $^{-1}$

### 3.2. Pure Zodiacal Spectra

Figure 3 shows a sample spectrum after removal of the contaminating atmospheric emission as described above. The abscissa is in units of radial velocity, where zero corresponds to the centroid of the unperturbed Mg I  $\lambda 5184$  component in the solar spectrum (Fig. 1). To obtain the centroid velocity (V), full width at half maximum (W), and area (A) of the zodiacal Mg I absorption component, a least squares three-gaussian fit, representing the Mg I and the two weak Fe I and Cr I features, was made to the spectrum. During the fit the relative centroid positions and the relative areas of the three components were held fixed at the values found in the twilight spectrum, and the widths of the two minor Fe I and Cr I features were held fixed at  $55 \text{ km s}^{-1}$ , the approximate mean broadening of the zodiacal spectra. The fitting procedure also took into account the  $12 \text{ km s}^{-1}$  wide instrumental response function of the WHAM spectrometer and a small correction for Doppler shifts due to the earth’s rotation. The resulting best fit (solid curve) and residuals are included in Figure 3. Values for the best fit parameters of the Mg I component for this and all the other spectra are listed in Table 1.

The resulting radial velocities, widths, and areas of the Mg I component along the ecliptic equator are plotted in Figures 4a, 4b, and 4c, respectively. The uncertainties associated with these results are the combined uncertainty associated with random errors due to Poisson noise, the placement of the continuum, plus the systematic error associated with the subtraction of the atmospheric emission. In this last case the error was estimated by fitting each spectrum two more times, after subtracting the “minimal” and the “maximal” versions of the atmospheric emission spectrum (Fig. 2c). We found that the uncertainty in the radial velocity is dominated by the systematic error associated with the removal of the atmospheric emission and that errors in the widths and areas are dominated by the uncertainty in the placement of the continuum. The uncertainties listed in Table 1 and plotted in Figures 4a and 4b below indicate only the systematic error due to the removal of the atmospheric emission. In most observations, the subtraction of the “minimal” (“maximal”) terrestrial spectrum instead of the “best” terrestrial spectrum results in systematically less (more) positive centroid velocities, narrower (wider) line widths, and slightly larger (smaller) areas. Also plotted are the resulting velocities (open squares in Fig. 4a) when *no* correction was made for the atmospheric emission, to illustrate the significant effect this emission can have on the derived results if it is not removed from the spectra. The effect on W and A is less dramatic, due in part to the fact that, while some of the emission lines fill in the zodiacal absorption profile slightly, other lines raise the “continuum”. The scatter in the values for the line widths and areas, which is significantly larger than the plotted (systematic) error, reflects primarily the uncertainties in W and A associated with continuum placement.

Figure 4a reveals a well-characterized velocity vs. elongation kinematic signature for the line centroids indicative of prograde orbits, and Figure 4b shows significant broadening of the line profiles with respect to the unperturbed solar spectrum at all elongations, including  $180^\circ$ . The radial velocities pass through zero at  $\epsilon \approx 54^\circ$ , near  $180^\circ$ , and at  $\epsilon \approx 315^\circ$ , indicating a small ( $10^\circ$ ) evening–morning asymmetry in the elongation at which the radial velocity passes through zero. These data show no evidence for a general outflow (i.e., a mean positive velocity shift at  $180^\circ$ ) or an evening–morning asymmetry in the velocity amplitudes as reported in some earlier studies (East & Reay 1984; Hicks et al. 1974). Within the uncertainty associated with the removal of the atmospheric emission (see above), the radial velocity at  $180^\circ$  is consistent with zero and the maximum amplitudes of the radial velocities are anti-symmetric, reaching approximately  $+13 \text{ km s}^{-1}$  at  $\epsilon \approx 100^\circ$  and approximately  $-12 \text{ km s}^{-1}$  at  $\epsilon \approx 260^\circ$ . The area of the Mg I absorption profile is a tracer of the zodiacal continuum intensity, and Figure 4c shows evidence for the Gegenschein and the steep rise in zodiacal intensity for directions within about  $70^\circ$  of the sun. The absolute intensity calibration of these observations is accurate to only about 20%, and zero intensity relative to the continuum is uncertain due to an added flat continuum from parasitic (out of band) light. Because the intensity distribution of the zodiacal light has been well studied by others, the remainder of this paper focuses on some of the implications of the new kinematic information revealed by the radial velocities and line widths of the Mg I profile presented in Figures 4a and 4b.

## 4. DISCUSSION

### 4.1. Orbital Eccentricities

The orbital properties of the zodiacal dust, including the eccentricity, inclination, and the effect of radiation pressure, can be explored by comparing these results with line profiles and Doppler shifts calculated from models of the distribution, kinematics, and scattering properties of the dust (e.g., James 1969; Bandermann & Wolstencroft 1969; Rodriguez & Magro 1978; Hirschi 1985; Hirschi & Beard 1987; Mukai & Mann 1993; Clarke et al. 1996). In Figure 5 the observed velocity centroids V and line widths W are compared with models by Hirschi & Beard (1987) and Hirschi (1985), who have made the most detailed predictions of these two parameters. They considered a variety of models with isotropically scattering particles in prograde orbits confined to the ecliptic plane. We consider four of their models here: a) particles on circular orbits and influenced only by solar gravity, b) particles on elliptical orbits having a uniform distribution of eccentricities between 0 and 1, c) particles on elliptical orbits with a distribution of eccentricities weighted toward low eccentricities,

and d) particles on circular orbits but influenced by radiation pressure, that is, feeling a lower effective gravity. These models are represented by the solid, dotted, dot-dashed, and dashed curves, respectively, in Figure 5.

The data clearly rule out pure circular orbits (model a; solid line). The predicted amplitude of the radial velocity variations is too small, the elongations at which the predicted radial velocity curve passes thorough zero are too far from the sun, and the widths of the predicted profiles are too narrow to fit the observations. Particles in circular orbits, but moving at sub-Keplerian speeds due to radiation pressure (model d; dashed line), would exhibit a larger radial velocity amplitude and intercept zero velocity closer to the sun (Fig. 5a), depending on the magnitude of the effect. However, the predicted line widths from such circularly orbiting dust would still remain far too narrow to fit the observations (Fig. 5b).

These results agree best with models in which the zodiacal dust is moving on elliptical orbits. This conclusion is supported most convincingly by the observed broadening of the line profiles. As pointed out by Hirschi & Beard (1987), it is the line widths, especially near elongation  $180^\circ$ , that clearly distinguish spectra of elliptically orbiting dust from spectra of dust in circular orbits, including dust in circular orbits experiencing radiation pressure. Figures 4b and 5 and Table 1 show that the profiles are broadened significantly with respect to the unperturbed solar profile and with respect to profiles predicted by models in which the dust is only in circular orbits. For example, Figure 6 compares the average spectrum for the five observations within  $8^\circ$  of  $\epsilon = 180^\circ$  with the unperturbed solar spectrum. If all the orbits were circular and centered on the sun, the profiles would be nearly identical. The broadening of the zodiacal profiles can only be explained by particles having radial components to their orbital motion.

#### 4.2. Radiation Pressure and Orbital Inclinations

Orbital eccentricity alone is not sufficient to account for these observations. Although the predicted radial velocity variation from a dust population with a uniform distribution of orbital eccentricities (model b; dotted line) matches the observed radial velocities very well (Fig. 5a), the line widths predicted by this model are too large, especially near  $180^\circ$  (see Fig. 5b). The model that is weighted toward lower eccentricities (model c; dot-dashed) provides a much better fit to the observed widths overall; however, that model does not predict a velocity amplitude as large as is observed. Models that combine eccentric orbits (to account for the line width) with an influence from radiation pressure (to increase the velocity amplitude) appear to be needed to obtain the best fit to the observed velocity variations and the line widths simultaneously (see Table 3, column 2 in Hirschi & Beard 1987).

Another orbital parameter, which these models did not include, is inclination. Particles with a distribution of orbital inclinations will have smaller projected velocities along sightlines in the ecliptic plane. This will also increase the radial velocity amplitude (Rodriguez & Magro 1978) and thus mimic the effect of radiation pressure in observations confined to the ecliptic equator. Perhaps a combination of eccentricities and inclinations may even obviate the need for a significant effect from radiation pressure. The observations at high ecliptic latitude are therefore important for both probing the inclinations of the orbits and quantifying the influence of radiation pressure. Unfortunately, there are not yet models incorporating both eccentricity and inclination that predict both W and V.

A wide distribution of orbital inclinations is implied by the broad line profiles toward  $\epsilon \approx 272^\circ$ ,  $\beta \approx 47^\circ$  and the NEP (Table 1). The profile toward the NEP not only has one of the largest widths, but unlike profiles in all the other directions, has a distinctly flat-bottom shape. The NEP spectrum and the unperturbed solar spectrum are shown in Figure 7. This substantial broadening of the profile toward the ecliptic pole, greater than that toward the antisolar direction, implies a population of particles that have significant components of their orbital velocities projected perpendicular to the ecliptic plane. For an orbital speed of  $30 \text{ km s}^{-1}$  near 1 AU, and neglecting the radial motion associated with eccentricity, the approximately  $\pm 15 - 20 \text{ km s}^{-1}$  broadening at the base of the NEP profile suggests a distribution of inclinations extending up to about  $30^\circ - 40^\circ$  with respect to the ecliptic plane. This is close to, but somewhat broader than the distribution derived from the Galileo and Ulysses *in situ* interplanetary dust impact detectors (Grün et al. 1997).

### 4.3. Line Profile Asymmetries

After removal of the atmospheric emission and taking into account the weak solar Fe and Cr features on the red side of the Mg I line (Fig. 1), we see no pronounced asymmetries in the shape of the zodiacal profiles. This places additional constraints on the properties of the zodiacal dust. For example, the nature of the scattering phase function of the dust is uncertain (e.g., Hahn et al. 2002), and Clarke et al. (1996) have shown that significant profile asymmetries will be present if the scattering function derived by Hong (1985) is used instead of isotropic scattering. In particular, they predicted that profiles between  $\epsilon \approx 50^\circ - 70^\circ$  and in the corresponding interval at  $\epsilon \approx 290^\circ - 310^\circ$  would have clearly extended wings on the red and blue sides, respectively. Another source of profile asymmetry would be a population of dust in retrograde motion. James (1969) calculated the radial velocities that would be associated with particles on retrograde orbits and showed that they would produce a Doppler shifted absorption feature centered near  $+55 \text{ km s}^{-1}$  and  $-55 \text{ km s}^{-1}$  at  $\epsilon \approx 50^\circ - 70^\circ$  and

$\epsilon \approx 290^\circ - 310^\circ$ , respectively.

To search for these asymmetries, the mean spectrum within each of these two elongation intervals is plotted in Figure 8. To make the comparison easier the mean spectrum toward  $\epsilon \approx 50^\circ - 70^\circ$  was shifted  $9.0 \text{ km s}^{-1}$  to the blue so that the minima of the two profiles coincide. Within the scatter of the data points, the profile shapes appear to be nearly identical, indicating that there are no pronounced asymmetries produced by retrograde particles or the scattering discussed above. For example, the absence of a significant depression on the red side of the evening spectrum (open circles) relative to that part of the morning spectrum (filled circles), and *vice versa* for the blue side, indicate that any population of retrograde particles must be less than 10% the prograde population.

The spectra toward  $180^\circ$  and the NEP show marginal evidence for extra absorption on the red side of the profiles near  $+30 \text{ km s}^{-1}$  (Figs. 6 and 7). This could be an indication of a small population of particles with a radial outflow (Hirschi 1985); however, given current uncertainties associated with the removal of terrestrial emission (e.g., Fig. 6), it is difficult to judge its significance. A more extensive observational program, including studies of more than one Fraunhofer line, will be needed to characterize more accurately such subtle asymmetries (see below).

## 5. CONCLUSIONS AND FUTURE OBSERVATIONS

Observations of the Mg I  $\lambda 5184$  line with WHAM have demonstrated that high throughput spectroscopic measurements of scattered solar Fraunhofer line profiles in the zodiacal light can be a useful tool for exploring the properties of the zodiacal dust, as suggested by Ingham (1963), James (1969) and others. These observations, combined with models of the zodiacal cloud, have probed or placed constraints on the retrograde and prograde populations, the orbital eccentricities and inclinations, the effects of non-gravitational forces, and the scattering properties of the particles. Furthermore, this characterization of the Doppler distortions of Fraunhofer profiles in the zodiacal light should facilitate a more accurate removal of zodiacal contamination in other astrophysical observations (e.g., see Haffner et al. 2003). The detection of the extremely weak telluric emission lines also implies that caution must be used in the interpretation of line profiles, equivalent widths, line intensities, and the nature of the “continuum” in low resolution spectra of zodiacal light and other low surface brightness astrophysical sources.

These results also point to ways in which observations can be further improved. For example, integration times can be significantly lengthened to increase the signal-to-noise,

and the bandwidth of the spectra could be expanded to make it possible to define the continuum more accurately. A fuller sampling at higher ecliptic latitudes would also help to characterize more accurately particle orbits inclined to the ecliptic plane (Rodriguez & Magro 1978). Systematic errors associated with the removal of the atmospheric emission lines, the largest source of uncertainty in the measurements of radial velocities and profile shapes, could be reduced by observing two Fraunhofer lines (e.g., Mg I  $\lambda$ 5173 in addition to Mg I  $\lambda$ 5184). Both lines are modified identically by scattering from the zodiacal dust but are affected differently by the atmospheric foreground emission. A complete set of such spectra obtained multiple times over the course of a year or more would also allow a search for more subtle effects associated with possible azimuthal asymmetries in the zodiacal cloud, the inclination of the earth’s orbit with respect to the dust plane, and the eccentricity of the earth’s orbit (e.g., Dermott et al. 1994; Kelsall et al. 1998). In addition, because observations toward the same elongation at different times of the year sample different parts of the Milky Way, observations spread throughout the year could help to characterize and remove any spectral features associated with the background starlight (Mattila 1980). A more accurate unperturbed source spectrum (free of any “Ring effect”) could be obtained from observations of the moon, rather than the twilight sky. The WHAM facility provides an opportunity to carry out such an investigation. The proper interpretation of these data also requires a more complex grid of models, incorporating a range of orbital and scattering parameters and particle distributions (e.g., Haug 1958) that predict the velocities and shapes of the zodiacal line profiles over the sky.

## 6. ACKNOWLEDGMENTS

We thank Matt Haffner, Kurt Jaehnig, and Steve Tufte for their valuable contributions to the operation of WHAM, Alexander Kutyrev for his assistance and encouragement, and an anonymous referee for helpful comments. We are also grateful to Dean Hirschi for providing a copy of his PhD thesis. The WHAM program is supported by the National Science Foundation through grant AST-0204973.

## REFERENCES

- Bandermann, L. W. & Wolstencroft, R. D. 1969, Nature 221, 251
- Bernstein, R. A., Freedman, W. L., & Madore, B. F. 2002, ApJ 571, 85
- Clarke, D., Daehler, M., Mack, J. E., Ring, J., & Stoner, J. O. 1967, in Modern Astrophysics. A Memorial to Otto Struve, ed. M. Hack, (Gorden & Breach:New York; Gauthier-Villars:Paris), 43
- Clarke, D., Matthews, S. A., Mundell, C. G., & Weir, A. S. 1996, A&A 308, 273
- Daehler, M., Mack, J. E., Stoner, J. O., Clarke, D., & Ring, J. 1968, Planet. Space Sci. 16, 795
- Delbouille, L., Neven, L., & Roland, C. 1973, “Photometric Atlas of the Solar Spectrum from  $\lambda$ 3000 to  $\lambda$ 10000”, Institut d’Astrophysique de l’Universite de Liege, Observatoire Royal de Belgique
- Dermott, S. F., Jayaraman, S., Xu, Y. L., Gustafson, B. Å. S., & Liou, J. C. 1994, Nature, 369, 719
- East, I. R. & Reay, N. K. 1984, A&A 139, 512
- Fried, J. W. 1978, A&A 68, 259
- Grainger, J. F. & Ring, J. 1962, Nature 193, 762
- Grün, E., et al. 1997, Icarus 129, 270
- Haffner, L. M., Reynolds, R. J., Tufte, S. L., Madsen, G. J., Jaehnig, K., & Percival, J. 2003, ApJS, 149, 405
- Hahn, J. M., Zook, H. A., Cooper, B., & Sunkara, B. 2002, Icarus 158, 360
- Haug, U. 1958, ZAp (Zeitschrift für Astrophysik) 44, 71
- Hausen, N. R., Reynolds , R. J., Haffner, L. M., & Tufte, S. L. 2002, ApJ 565, 1060
- Hicks, T. R., May, B. H., & Reay, N. K. 1974, MNRAS 166, 439
- Hirschi, D. C. 1985, PhD Thesis, University of Kansas
- Hirschi, D. C. & Beard, D. B. 1987, Planet. Space Sci., 35, 1021

- Hong, S. S. 1985, A&A 146, 67
- Ingham, M.F. 1963, MNRAS 126, 378
- James, J. F., 1969, MNRAS 142, 45
- James, J. F. 1996, MNRAS 280, 1055
- James, J. F. & Smeethe, M. J. 1970, Nature 227, 589
- Kelsall, T., et al. 1998, ApJ 508, 44
- Mann, I. 1998, Earth Planets Space 50, 465
- Mann, I., Grün, E., & Wilck, M. 1996, Icarus, 120, 399
- Mattila, K. 1980, A&A 82, 373
- Morgenthaler, J. P., Harris, W. M., Scherb, F., Anderson, C. M., Oliverson, R. J., Doane, N.E., Combi, M. R., Marconi, M. L., & Smyth, W. H. 2001, ApJ 563, 451
- Mukai, T. & Mann, I. 1993, A&A 271, 530
- Nossal, S., Roesler, F. L., Bishop, J., Reynolds, R. J., Haffner, L. M., Tufte, S. L., Percival, J., & Mierkiewicz, E. Z. 2001, J. Geophys. Res. 106, 560
- Pallamraju, D., Baumgardner, J., & Chakrabarti, S. 2000, Geophy. Res. Lett. 27, 1875
- Reay, N. K. 1969, Nature 224, 54
- Reay, N. K. & Ring, J. 1969, Planet. Space Sci. 17, 561
- Reynolds, R. J., Roesler, F. L., & Scherb, F. 1973, ApJ 179, 651
- Rodriguez, G. L. & Magro, C. S. 1978, A&A 64, 161
- Sioris, C. E. & Evans, W. F. J. 1999, Appl. Opt. 38, 2706
- Tufte, S. L. 1997, PhD Thesis, University of Wisconsin-Madison

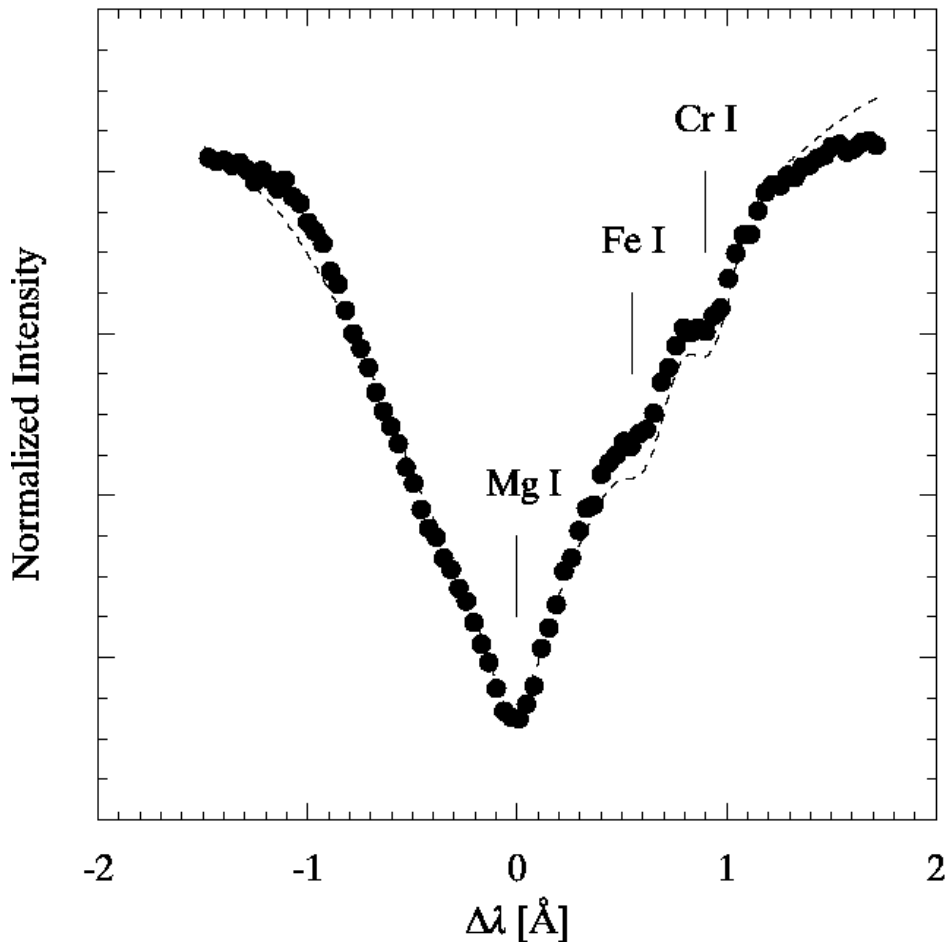


Fig. 1.— Unperturbed solar spectrum from the bright twilight sky (filled circles), showing the Mg I profile plus the two weaker, narrower lines from Fe I and Cr I. For comparison, the dashed curve shows the direct, high resolution solar spectrum from Delbouille, Neven, & Roland (1973) convolved with WHAM’s spectral response function (see §2).

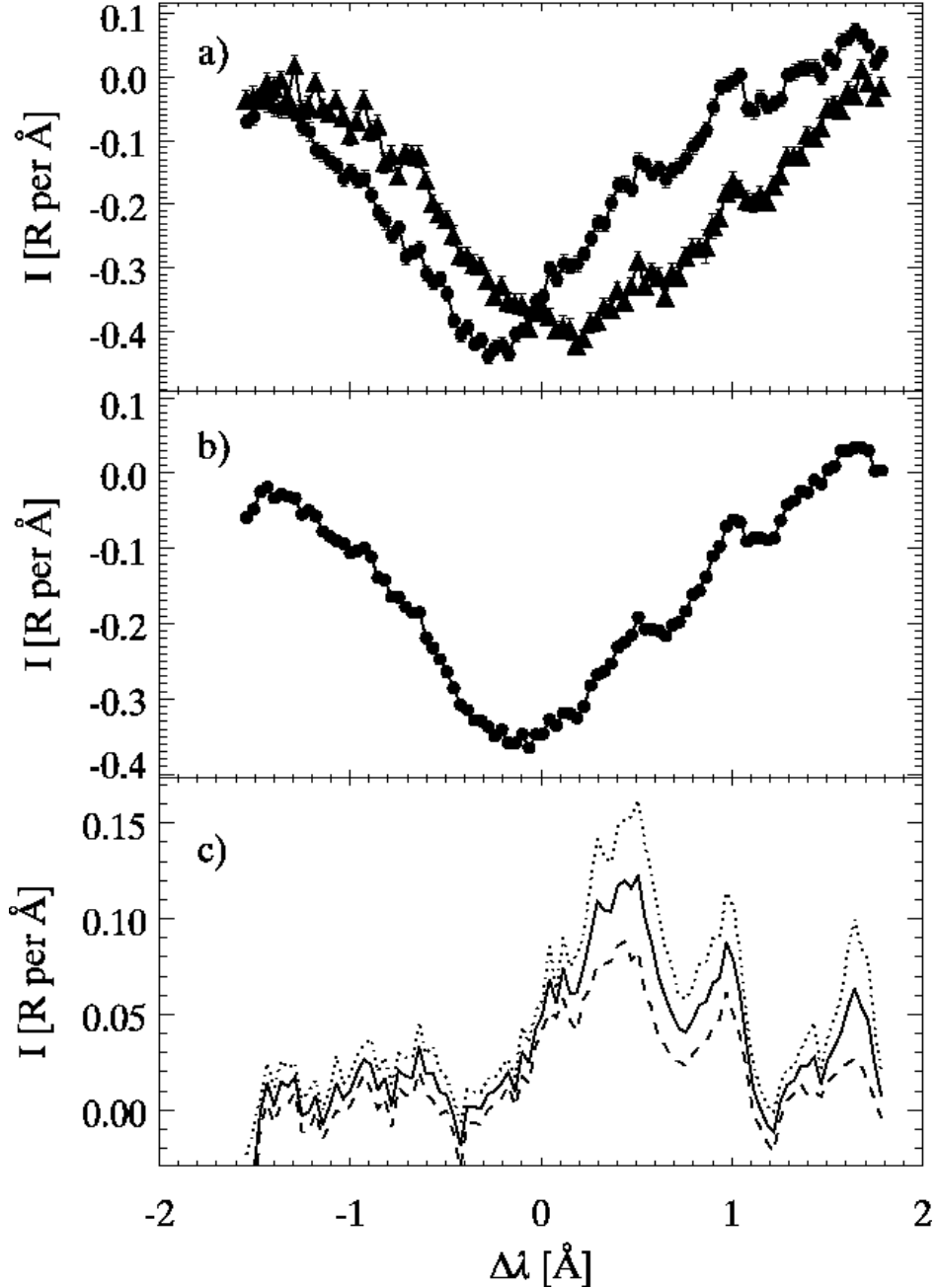


Fig. 2.— a) Average spectrum between  $\epsilon \approx 88^\circ - 108^\circ$  (circles) and the average spectrum between  $\epsilon \approx 252^\circ - 264^\circ$  (triangles), showing weak, narrow, unshifted terrestrial emission lines superposed on the scattered solar profile, broadened and shifted by the motion of the zodiacal dust. b) Average of all spectra between elongations  $88^\circ$  and  $264^\circ$ , which shows more clearly the contaminating terrestrial emission lines superposed on the kinematically smeared, high signal-to-noise zodiacal spectrum. c) “Best fit” (solid line) atmospheric emission spectrum extracted from the spectrum in Fig. 2b (see text). The dotted line represents the maximal atmospheric contamination and the dashed line the minimal atmospheric contamination consistent with the spectrum in Fig. 2b. 1 R per  $\text{\AA}$  corresponds to  $3 \times 10^{-7} \text{ erg cm}^{-2} \text{ s}^{-1} \text{ sr}^{-1} \text{ \AA}^{-1}$  at  $5184 \text{ \AA}$ .

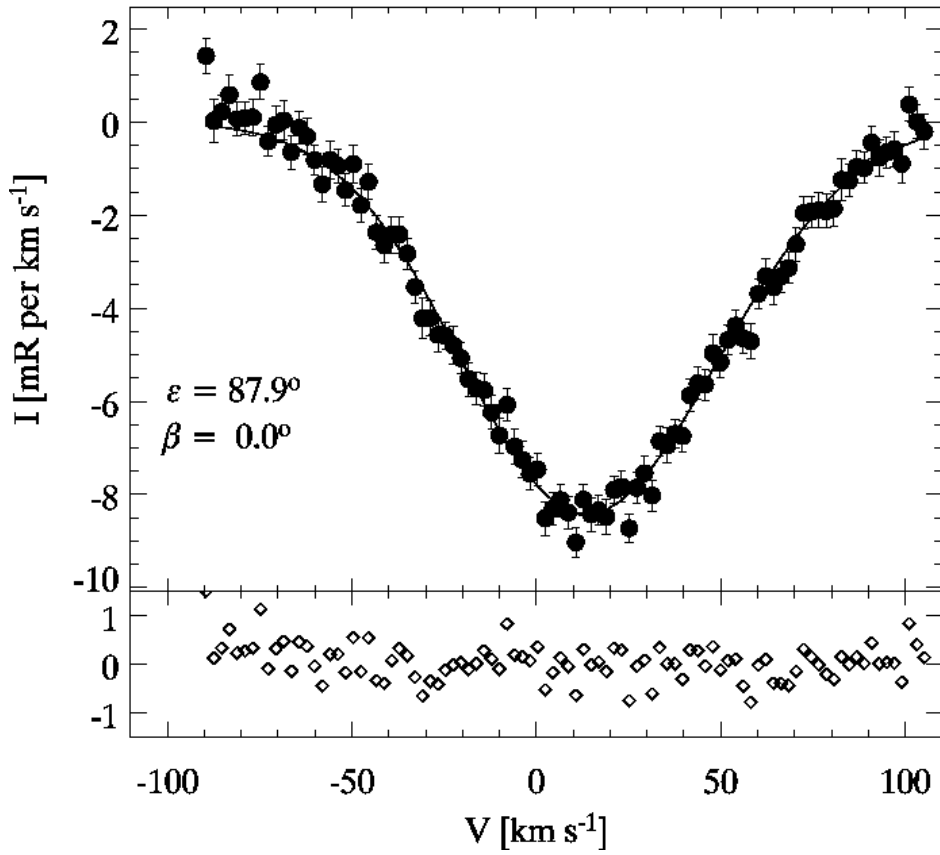


Fig. 3.— Sample spectrum of the zodiacal light toward  $\epsilon \approx 88^\circ$  with the terrestrial emission removed. The integration time was 600 s. The best three-gaussian (Mg I, Fe I, and Cr I) fit (solid line) and the resulting residuals are also indicated. The error bars represent the  $\pm 1\sigma$  Poisson noise.

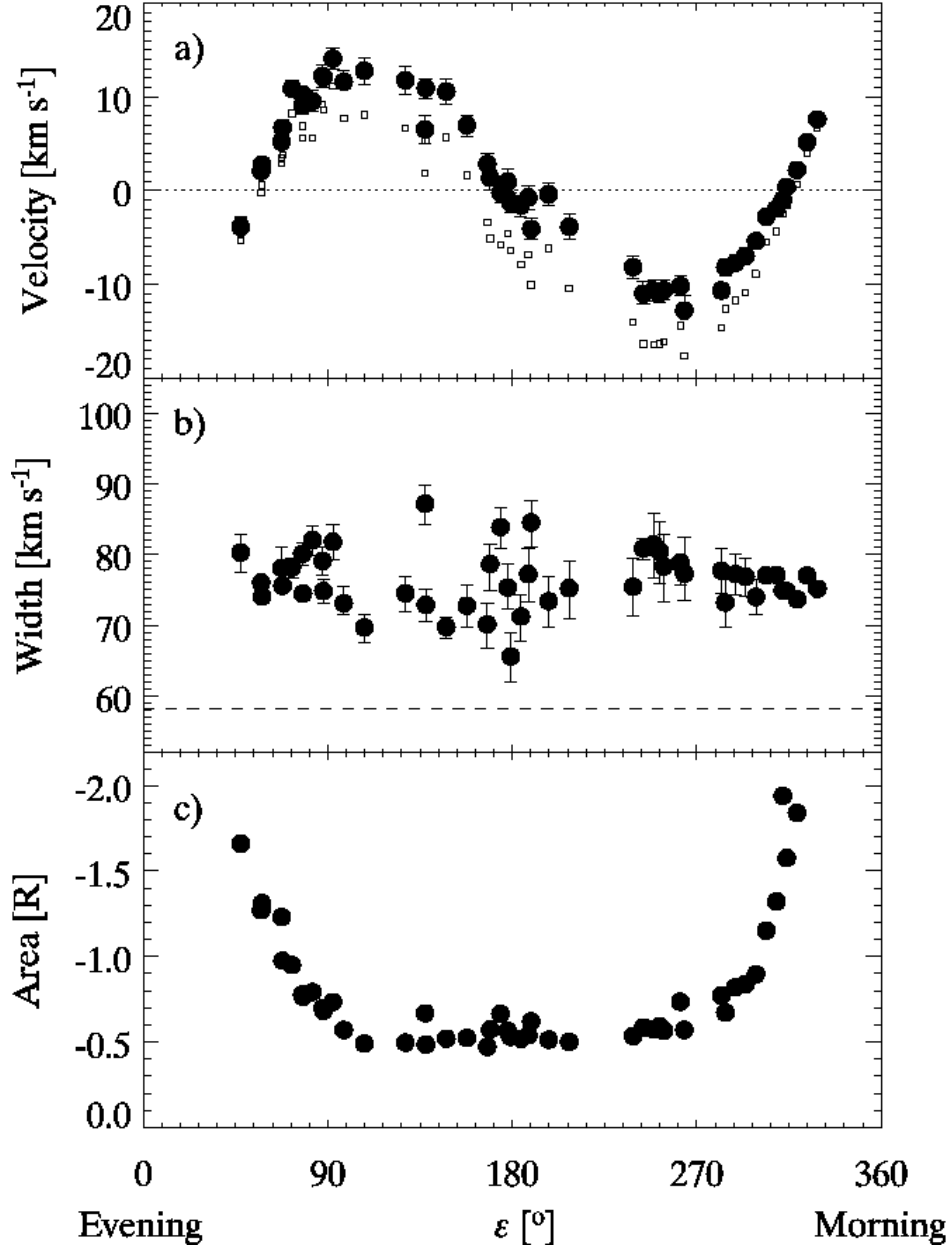


Fig. 4.— Best fit centroid radial velocity ( $V$ ), full width at half maximum ( $W$ ), and area ( $A$ ) for the Mg I line are plotted for each of the zodiacal spectra near the ecliptic equator. The error bars represent the systematic uncertainty listed in Table 1 associated with the removal of the contaminating atmospheric emission (see §3). The open squares in Fig. 4a show the resulting velocities if the atmospheric emission is not removed. The dashed line in Fig. 4b represents the width of the Mg I component in the unperturbed solar spectrum.

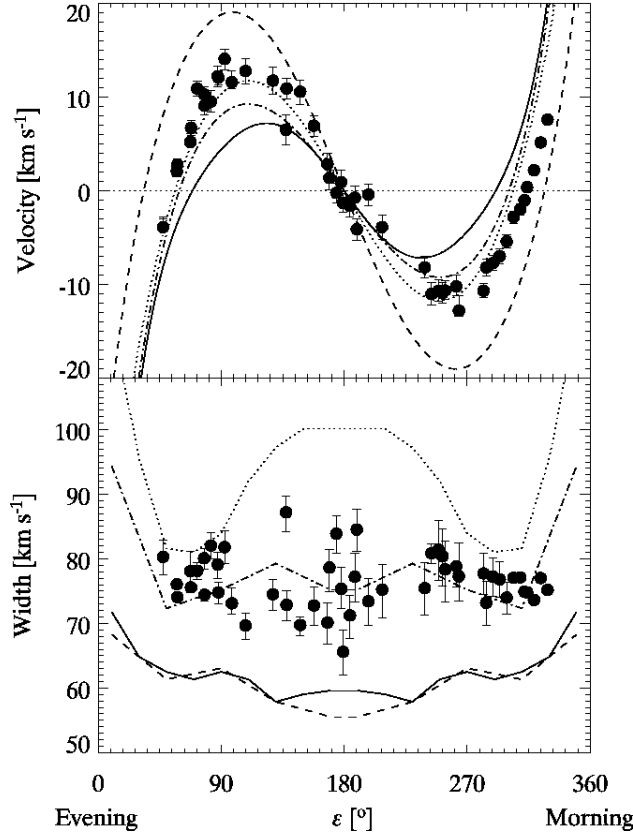


Fig. 5.— Predictions for the velocities and widths of the Mg I line from models of the zodiacal dust by Hirschi & Beard (1987) and Hirschi (1985): *solid line* (model a): particles on circular orbits and influenced only by solar gravity; *dotted line* (model b): particles on elliptical orbits with a uniform distribution of eccentricities between 0 and 1, randomly distributed perihelions and no radiation pressure; *dot-dashed line* (model c): similar to model b above, but weighted toward lower eccentricities such that  $n(e) \sim 1/e$ ; *dashed line* (model d): particles on circular orbits with a size distribution proportional to  $s^{-4}$  down to about  $0.5 \mu\text{m}$  and density  $1 \text{ g cm}^{-3}$ , resulting in a significant influence by solar radiation pressure that reduces the effective gravity. In all models the particle motion is parallel to the ecliptic plane, and in models a, b, and c, the particle number density decreases with distance from the sun as  $n(r) \sim r^{-1.5}$ ; taken from Table 2 in Hirschi & Beard (1987). For model d,  $n(r) \sim r^{-2}$ , and the velocities are taken from Table 4 in Hirschi (1985). A seventh order polynomial passing through all the model data points was used to interpolate between model values for velocities.

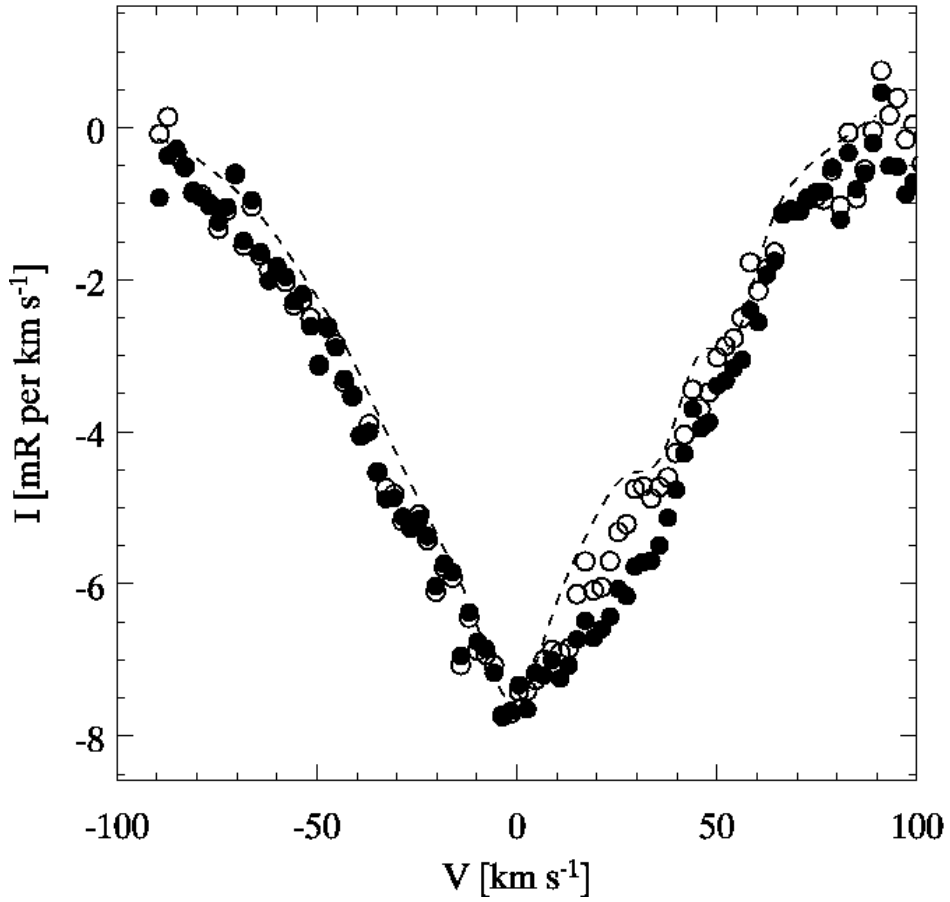


Fig. 6.— Mean spectrum for  $\epsilon \approx 174^\circ - 188^\circ$ , showing that the antisolar zodiacal profile is broadened relative to the unperturbed solar profile (convolved direct solar spectrum; dashed curve). The filled and open symbols represent the profile with maximal and minimal corrections for the atmospheric contamination, respectively (see §3.1 and Fig. 2c). The “continua” and minima of the profiles were made to coincide.

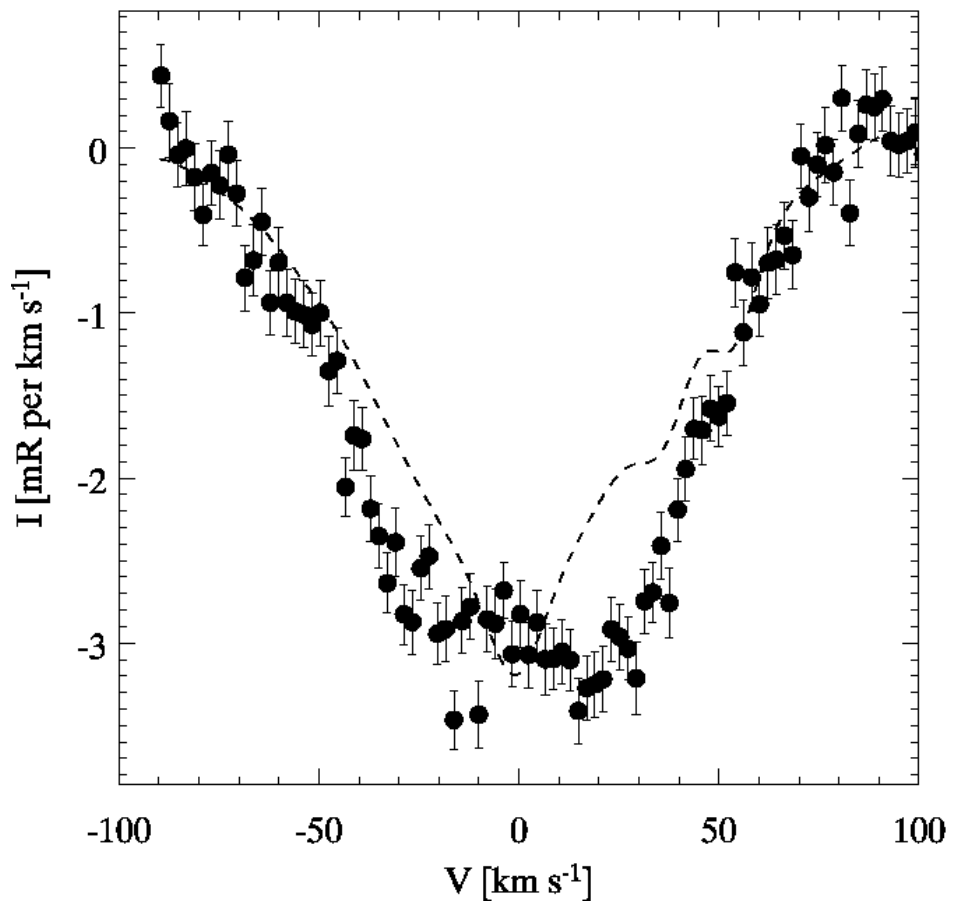


Fig. 7.— Zodiacal spectrum toward the north ecliptic pole (NEP). The unperturbed solar profile is included for comparison. The error bars represent the  $\pm 1\sigma$  Poisson noise.

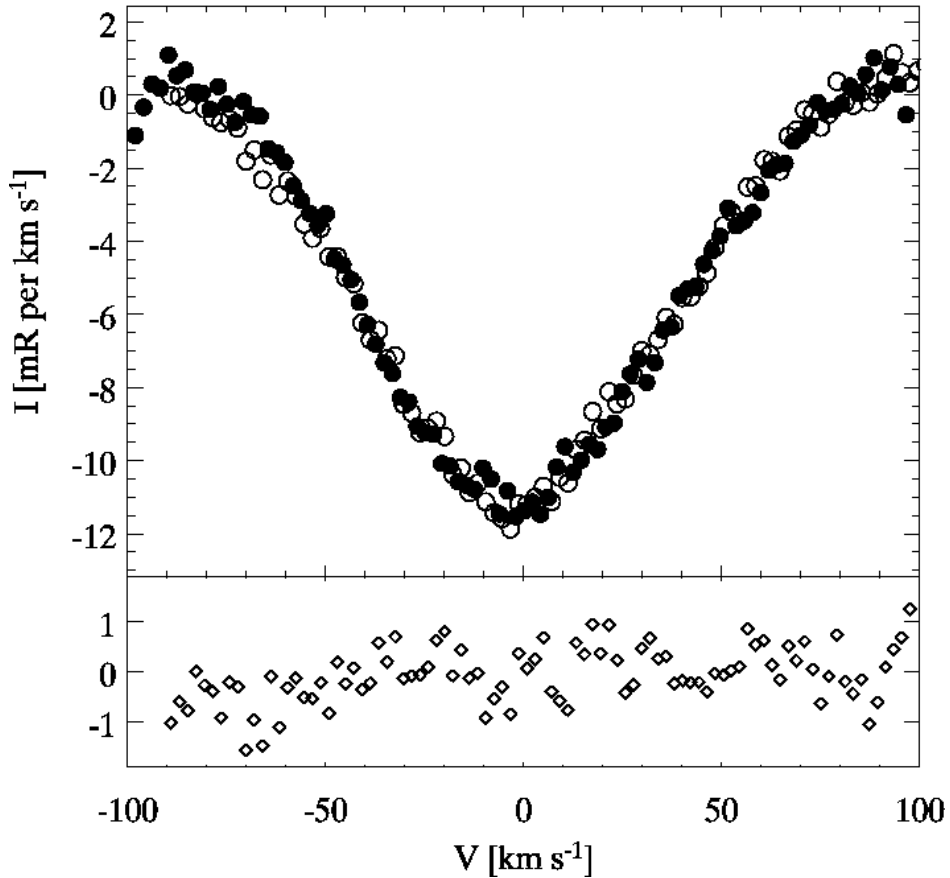


Fig. 8.— Average spectrum between  $\epsilon \approx 50^\circ$  and  $70^\circ$  (open symbols) and the average spectrum between  $\epsilon \approx 290^\circ$  and  $310^\circ$  (filled symbols) have been superposed to search for asymmetries in the line profiles (see §4.3). To make the comparison easier, the former spectrum was shifted  $-9.0 \text{ km s}^{-1}$  with respect to the latter spectrum. The difference between the two profiles is also plotted (open diamonds).

Table 1. Summary of Observations and Results

$\epsilon$ (°)	$\beta$ (°)	Time (sec)	V (km s <sup>-1</sup> )	$\Delta V_{min}^a$ (km s <sup>-1</sup> )	$\Delta V_{max}^a$ (km s <sup>-1</sup> )	W (km s <sup>-1</sup> )	$\Delta W_{min}^a$ (km s <sup>-1</sup> )	$\Delta W_{max}^a$ (km s <sup>-1</sup> )	A (R)	$\Delta A_{min}^a$ (R)	$\Delta A_{max}^a$ (R)
47.5	0.0	240	-3.4	-0.5	+0.5	80.3	-1.4	+1.3	-1.67	-0.04	+0.05
57.5	0.0	120	+2.1	-0.6	+0.7	76.1	-0.3	+0.5	-1.27	-0.01	+0.03
57.9	0.0	600	+2.8	-0.6	+0.6	74.1	-0.2	+0.2	-1.31	-0.01	+0.01
67.5	0.0	240	+5.7	-0.6	+0.5	78.1	-1.3	+1.3	-1.24	-0.04	+0.04
67.9	0.0	600	+6.7	-0.8	+0.8	75.6	+0.3	-0.4	-0.98	0.00	0.00
72.5	0.0	120	+10.9	-0.8	+0.8	78.2	+1.3	-1.4	-0.95	0.01	-0.01
77.5	0.0	120	+10.3	-0.8	+0.8	80.1	-1.6	+1.5	-0.78	-0.04	+0.04
77.9	0.0	1800	+9.1	-1.0	+1.0	74.4	+0.7	-0.9	-0.77	0.00	0.00
82.5	0.0	120	+9.5	-1.1	+1.1	82.1	+2.0	-2.1	-0.79	0.01	-0.01
87.5	0.0	120	+12.2	-1.2	+1.1	79.1	+1.9	-2.1	-0.70	0.01	-0.01
87.9	0.0	600	+12.1	-0.8	+0.7	74.8	-1.7	+1.6	-0.68	-0.04	+0.04
92.5	0.0	120	+14.1	-1.1	+1.1	81.8	+2.5	-2.6	-0.73	0.01	-0.01
97.8	0.0	600	+11.6	-0.7	+1.2	73.1	-1.6	+2.4	-0.57	-0.04	+0.05
107.8	0.0	600	+12.8	-1.4	+1.3	69.7	+1.9	-2.2	-0.49	0.00	0.00
127.9	0.1	600	+11.7	-1.5	+1.4	74.5	+2.3	-2.5	-0.50	0.00	-0.01
137.5	0.0	120	+6.5	-1.6	+1.6	87.2	+2.6	-3.0	-0.67	0.02	-0.02
137.8	0.0	600	+10.9	-1.1	+1.0	72.9	-2.4	+2.2	-0.49	-0.04	+0.04
147.8	0.0	600	+10.5	-1.3	+1.3	69.8	+1.3	-1.6	-0.52	0.00	0.00
157.8	0.0	600	+6.9	-1.2	+1.1	72.8	-3.1	+2.8	-0.52	-0.04	+0.04
167.8	0.0	600	+2.8	-1.2	+1.2	70.1	-3.4	+3.0	-0.47	-0.04	+0.04
169.2	0.0	120	+1.4	-1.3	+0.8	78.7	-3.7	+2.8	-0.57	-0.05	+0.04
174.2	0.0	120	-0.3	-1.1	+1.0	83.9	-3.0	+2.8	-0.66	-0.04	+0.05
177.8	0.0	600	+0.9	-1.0	+1.3	75.4	-3.0	+3.3	-0.56	-0.04	+0.05
179.3	0.0	120	-1.3	-1.0	+1.0	65.6	-3.6	+3.4	-0.53	-0.04	+0.04

Table 1—Continued

$\epsilon$ (°)	$\beta$ (°)	Time (sec)	V (km s <sup>-1</sup> )	$\Delta V_{min}^a$ (km s <sup>-1</sup> )	$\Delta V_{max}^a$ (km s <sup>-1</sup> )	W (km s <sup>-1</sup> )	$\Delta W_{min}^a$ (km s <sup>-1</sup> )	$\Delta W_{max}^a$ (km s <sup>-1</sup> )	A (R)	$\Delta A_{min}^a$ (R)	$\Delta A_{max}^a$ (R)
184.2	0.0	120	-1.6	-1.2	+1.0	71.2	-3.6	+3.1	-0.52	-0.04	+0.04
187.8	0.0	600	-0.8	-1.2	+1.2	77.2	-3.9	+3.6	-0.54	-0.04	+0.04
189.2	0.0	120	-4.1	-1.1	+1.1	84.5	-3.4	+3.1	-0.62	-0.04	+0.04
197.8	0.0	600	-0.4	-1.2	+1.1	73.4	-3.7	+3.5	-0.51	-0.04	+0.04
207.8	0.0	600	-3.9	-1.3	+1.3	75.2	-4.3	+3.9	-0.50	-0.04	+0.04
239.0	2.0	300	-8.2	-1.2	+1.2	75.4	-4.2	+4.0	-0.53	-0.04	+0.04
244.0	2.0	300	-11.0	-1.2	+1.3	80.9	-1.6	+1.5	-0.59	-0.01	+0.01
249.0	2.0	300	-10.7	-1.1	+1.2	81.4	-4.7	+4.5	-0.57	-0.04	+0.05
252.1	0.0	600	-10.9	-1.1	+1.1	80.4	-4.6	+4.3	-0.59	-0.04	+0.05
254.0	2.0	300	-10.7	-0.9	+1.1	78.4	-5.0	+4.5	-0.57	-0.04	+0.04
262.1	0.0	1800	-10.2	-0.9	+1.2	78.8	-1.2	-3.2	-0.74	-0.01	-0.06
264.0	2.0	300	-12.8	-0.6	+1.6	77.3	-3.9	+5.2	-0.57	-0.04	+0.05
282.0	0.0	600	-10.7	-0.8	+0.8	77.7	-3.2	+3.2	-0.77	-0.04	+0.04
283.9	2.0	300	-8.2	-0.9	+0.9	73.2	-3.5	+3.3	-0.67	-0.04	+0.04
288.9	2.0	300	-7.7	-0.8	+0.8	77.2	-3.0	+2.9	-0.82	-0.04	+0.04
293.9	2.0	300	-7.0	-0.8	+0.8	76.8	-2.8	+2.7	-0.84	-0.04	+0.04
298.9	2.0	300	-5.4	-0.7	+0.7	74.0	-2.6	+2.4	-0.90	-0.04	+0.04
303.9	2.0	300	-2.8	-0.6	+0.7	77.1	-0.5	+0.4	-1.15	-0.01	+0.01
308.9	2.0	300	-2.0	-0.6	+0.6	77.2	-0.4	+0.3	-1.32	-0.01	+0.01
312.0	0.0	600	-1.0	-0.4	+0.4	74.9	-0.3	+0.3	-1.94	-0.01	+0.01
313.9	2.0	300	+0.4	-0.5	+0.5	74.8	-0.3	+0.2	-1.58	-0.01	+0.01
318.9	2.0	300	+2.2	-0.4	+0.4	73.6	-0.2	+0.1	-1.84	-0.01	+0.01
323.8	2.0	300	+5.1	-0.3	+0.3	77.0	+0.1	-0.1	-2.45	-0.00	0.00
328.9	2.0	300	+7.6	-0.2	+0.2	75.2	+0.1	-0.1	-3.07	-0.00	+0.01

Table 1—Continued

$\epsilon$ (°)	$\beta$ (°)	Time (sec)	V (km s <sup>-1</sup> )	$\Delta V_{min}^a$ (km s <sup>-1</sup> )	$\Delta V_{max}^a$ (km s <sup>-1</sup> )	W (km s <sup>-1</sup> )	$\Delta W_{min}^a$ (km s <sup>-1</sup> )	$\Delta W_{max}^a$ (km s <sup>-1</sup> )	A (R)	$\Delta A_{min}^a$ (R)	$\Delta A_{max}^a$ (R)
333.9	2.0	300	+8.5	-0.2	+0.2	76.1	+0.1	-0.1	-5.06	0.00	0.00
NEP	90.0	2580	-2.2	-2.5	+2.5	83.2	+0.4	-0.4	-0.36	0.00	+0.01
272	47	1800	-3.2	-2.1	+2.1	77.3	+1.4	-1.4	-0.39	+0.01	-0.01
Twil	ight	...	0.0	...	...	58.2	...	...	...	...	...

<sup>a</sup> $\Delta X_{min}$  ( $\Delta X_{max}$ ) is the change in the corresponding value if the minimal (maximal) correction is used for the atmospheric lines, i.e.  $\Delta X_{min} = X_{min} - X$  (see §3)